
# BRNO UNIVERSITY OF TECHNOLOGY

VYSOKÉ UČENÍ TECHNICKÉ V BRNĚ

## FACULTY OF MECHANICAL ENGINEERING

FAKULTA STROJNÍHO INŽENÝRSTVÍ

## INSTITUTE OF SOLID MECHANICS, MECHATRONICS AND BIOMECHANICS

ÚSTAV MECHANIKY TĚLES, MECHATRONIKY A BIOMECHANIKY


# DEVELOPMENT OF A METHODOLOGY FOR FATIGUE CRACK LENGTH DETERMINATION USING DIGITAL IMAGE CORRELATION

VÝVOJ METODIKY PRO STANOVENÍ DÉLKY ÚNAVOVÉ TRHLINY POMOCÍ KORELACE DIGITÁLNÍCH OBRAZŮ

**CONDENSED VERSION OF DOCTORAL THESIS**

ZKRÁCENÁ VERZE DISERTAČNÍ PRÁCE


AUTHOR — Ing. Bořek Ščerba

AUTOR PRÁCE

SUPERVISOR — doc. Ing. Tomáš Návrat, Ph.D.

ŠKOLITEL



BRNO 2025

## Keywords (alphabetical order)

Crack opening displacement (COD) profile; Digital image correlation (DIC) for fatigue testing; Fatigue crack length measurement in metals; Fatigue crack growth rate evaluation; Inflection point method for crack-tip localization (IPM); Strain threshold method (STM); Virtual extensometers for crack monitoring; Visual inspection with a traveling microscope (VIM).

## Klíčová slova

Otevření trhliny (COD); Korelace digitálních obrazů (DIC), Měření délky únavové trhliny v kovech; Vyhodnocení rychlosti růstu únavové trhliny; Metoda inflexního bodu pro lokalizaci čela trhliny (IPM); Metoda prahového přetvoření (STM); Virtuální extenzometry pro monitorování trhliny; Vizuální kontrola posuvným mikroskopem (VIM).

## Místo uložení práce

Vysoké učení technické v Brně

Fakulta strojního inženýrství

Technická 2896/2

616 69 Brno

# Content

# 1 Introduction

Many traditional methods for measuring crack length have been developed, continuously improved, and remain widely used for both monotonic and cyclic tests. Examples of these methods include the compliance method, the electric potential drop technique, the foil strain-gauge approach, the crack opening displacement (COD) technique, and the widely used Visual Inspection Method (VIM) among non-contact techniques.

When VIM is used to determine the crack length in a fatigue test, a traveling microscope or an equivalent magnifying device is used to locate the crack tip. The crack tip position is determined using, for example, a fine optical grid pre-applied to the specimen [1] or a digital indicator integrated with the optical device [2]. This is performed manually; the technician must stop the test to take the measurements. This conventional non-contact method raises the question of whether crack length can be measured without stopping the test, as recommended by the relevant standard [3]. Achieving this could reduce operator workload, simplify the measurement process, and enable greater automation. Digital image correlation (DIC) may provide a solution to this problem.

This thesis develops a DIC-based methodology that replaces VIM and validates it against VIM data across materials, specimen sizes/types, and load levels, while also comparing it with a DIC thresholding approach—the strain-threshold method (STM). Sensitivity to input parameters is analyzed, limitations are identified, and user recommendations are provided. The core estimator is a physics-based Inflection point method (IPM) and its fast, filtered implementation (fIPMf).

# 2 State of the Art: DIC Crack Length Measurement

The review shows that some studies employ advanced techniques such as 3D DIC [4] or DVC [5], which require significant investments in hardware and software when using commercial solutions. Additionally, DVC is quite impractical for real-time measurements. However, most of the studies found (for example [6], [7], [8], [9]) utilize only 2D DIC full-field measurements.

Employing 2D DIC full-field measurements is a flexible and comprehensive approach for fatigue testing, as it can be used even when the crack does not propagate in a straight line. On the other hand, it can be computationally demanding to achieve sufficient accuracy, since it requires computing many points in the DIC mesh. Therefore, a common practice to achieve reasonable temporal and spatial resolution is to perform calculations in post-processing on the recorded images.

The standard for testing fatigue crack growth rates (FCGR) mandates that the crack must propagate in a straight line, and any significant deviation renders the test invalid [3]. Therefore, it is possible to simplify the 2D full-field measurement to the 1D DIC approach [10]. This technique focuses exclusively on extracting deformations along the anticipated crack path, thereby reducing the number of points where DIC calculations are performed. Consequently, computational time is reduced, enhancing usability for real-time applications. Real-time response is essential to enable the potential automation and control of cyclic tests using DIC.

The 1D DIC approach for extracting the COD curve has been used in far fewer studies, for example in [11], [12], [13], [14]. Although this technique significantly reduces computational demands, it is often stated that the crack-tip location corresponds to the coordinate where the COD reaches zero or a certain threshold value, but locating the crack tip is not straightforward; for example: “crack tip cannot be easily located from the opening profile $COD_{DIC}$” [15]. For the zero-COD approach, the measurements in this thesis indicate that the transition of the COD to zero is very gradual and noisy, making it challenging to determine the exact zero point.

To assess crack length, most 2D full-field and 1D DIC approaches use a threshold value to determine the crack and its tip, whether based on displacement, strain, or grayscale gradient. When deformation is used as the threshold quantity ($y_{th}$), the author refers to this as the deformation threshold method (DTM) [10], schematically illustrated in Fig. 1. 1D DIC using DTM can also be found in commercial DIC systems, such as those by Imetrum [16] or X-Sight [17].

This phenomenological approach is easy to implement, which supports its wide use. However, the primary difficulty in practice is selecting the threshold value, which can vary with material properties, specimen size and type, and especially the applied load level. This variability may necessitate a threshold database customized for specific use cases. The load-level dependence is particularly problematic, as load changes not only between tests but also within a single test to evaluate FCGR at different stress-intensity-factor (SIF) values and to identify the SIF threshold when the crack does not grow. This limitation is significant, motivating a different approach that better reflects the measured phenomenon.

The phenomenon is clarified by the works of Barenblatt [18] and Dugdale [19], who pioneered the concept of molecular cohesive forces ahead of the crack tip. In their model, opposing crack faces attract strongly at small separations, and this attraction weakens as separation increases, leading to the cusp-like shape formed by the gradually approaching crack faces. When the crack shape is represented (e.g., via COD), the transition between the region where cohesive forces act (process zone) and the region without them is marked by an inflection point (IP), as illustrated in Fig. 1. According to several sources that account for cohesive forces, such as [20], [21], [22] and [23], the crack tip is situated at the boundary of these two regions and defines the crack length. This will be referred to as inflection-point principle.

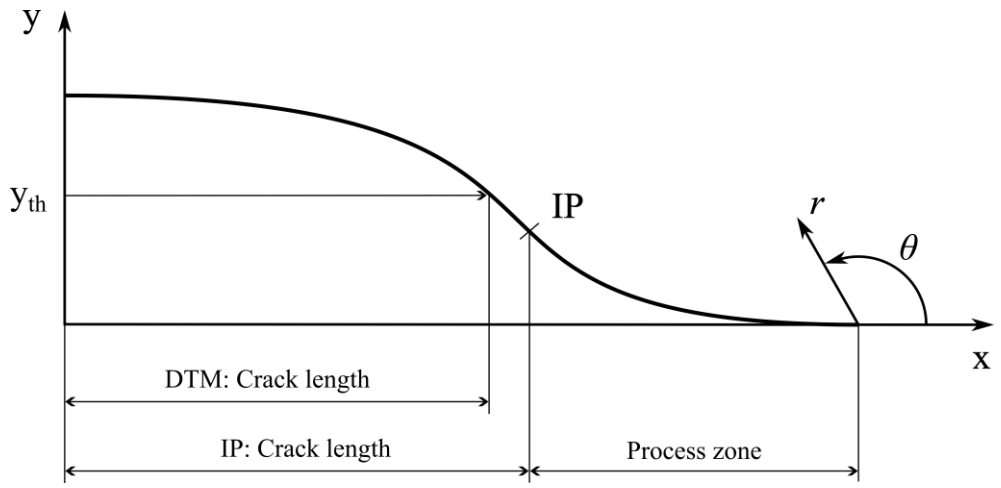


*Fig. 1: The configuration of the open crack, where the x-axis denotes the distance from the notch tip, and the y-axis indicates the displacement (e.g. COD), highlighting the inflection point. The crack's shape is symmetric relative to the x-axis, with only one side depicted. On the right, the radial coordinate system (r, θ) used for deformation calculations [27] is presented, while the concept of the deformation threshold method is shown on the left, with $y_{th}$ signifying the threshold value [10]*

Applying this principle to practical fatigue crack length determination using DIC, only one study [24] was found that identifies the IP on the COD curve. The study, focusing on polymers, suggests a correlation between the crack-tip location and the IP position in DIC-measured data on a CT sample. However, its reliability appears limited due to the methodology: the comparison uses VIM with a traveling microscope on the side opposite the DIC camera, so results may differ due to uneven through-thickness growth. The paper acknowledges this and recommends performing comparisons on the same specimen side. Additionally, it does not provide details about the DIC algorithm settings or the methods used to extract the IP.

# 3 Problem Statement and Objectives

Considering the outcomes of the literature review and the inflection-point principle, which together outline the state of the art and research gaps in DIC crack length measurement, the following **problem** is formulated:

*Development of a DIC-based methodology for real-time fatigue crack length measurement of metals.*

The methodology will incorporate a novel method for crack length assessment from 1D DIC data, which is physics-based, unlike the currently used DTM, and does not require a threshold value. This will enhance the versatility and applicability of DIC in the crack length measurement of metallic materials. It can replace the VIM widely used in fatigue testing, enabling measurement and quick assessment of results without stopping the cycling. This will make testing more efficient and create opportunities for future automation and control of the tests.

To successfully address the identified research gaps, the following **objectives** must be fulfilled:

- *Creation of a methodology for determining fatigue crack length using digital image correlation (DIC).*
- *Validation of the created methodology using a currently utilized non-DIC approach for determining fatigue crack length. The validation will include various metallic materials, sample sizes, and load levels.*
- *Comparison of the created methodology with another currently used DIC-based approach.*
- *Investigation of the methodology's response to changes in input parameters.*

# 4 Cornerstone of the Proposed Methodology

The cornerstone of the methodology for crack length determination is a novel approach to crack length assessment using DIC and artificial intelligence, named the Inflection point method (IPM) [10], which was published in *Theoretical and Applied Fracture Mechanics* in the article *Inflection point principle combined with digital image correlation and machine learning for crack length measurement in fatigue tests*.

The IPM is based on the inflection point principle, which has not yet been thoroughly validated for use with DIC data from fatigue tests of metallic materials. Therefore, this chapter validates the IPM and its underlying principle for accuracy, robustness, and feasibility under uninterrupted testing.

The VIM serves as the baseline (reference) method for assessing the accuracy of the IPM. The feasibility of continuous (uninterrupted) application is evaluated by collecting data during ongoing tests and assessing the accuracy of those results. Additionally, the STM is applied as a benchmark, representing a commonly used DIC-based approach, to provide a comprehensive comparison with the IPM.

## 4.1 Experimental Program for IPM Development

The initial experimental program was designed with the final methodology in mind but includes adjustments to obtain high-quality data for validating the IPM and comparing it with a different DIC-based approach. Specific details of these adjustments are provided in the following subsections.

To ensure robust validation, the program considers the effects of different metals, sample thicknesses, and load levels. Special attention is given to load level changes, as the STM is extremely sensitive to this factor.

### 4.1.1 Materials, Geometry, and Preparation

Standard CT samples according to the ASTM E647 [3] were used. The selected materials represent a range of commonly inspected metallic materials at the testing facility of the Institute of Physics of Materials of the Czech Academy of Sciences (hereafter *Facility*): low alloy steel 38MnVS6, stainless steel 1.4306, and aluminum alloy EN AW-7075. To include different specimen sizes, the thickness (B) differed for the 1.4306 specimen, as this affects the constraint at the crack tip and thus might affect the behavior of the IPM. The specimen specifications are summarized in Tab. 1.

*Tab. 1: Overview of standard CT samples for the experiment [10]*

| *Material* | *Piece No.* | $W^a$ *[mm]* | $B^b$ *[W]* | $a_n{}^c$ *[W]* | *Notch type* | $P_{max}{}^d$ *[kN]* |
|---|---|---|---|---|---|---|
| 38MnVS6 | 1 | 50 | 0.2 | 0.25 | Chevron | 6.5 |
| 38MnVS6 | 2 | 50 | 0.2 | 0.25 | Chevron | 5.5 |
| 1.4306 | 1 | 50 | 0.1 | 0.25 | Chevron | 10.8 |
| 1.4306 | 1 | 50 | 0.2 | 0.25 | Chevron | 7.2 |
| 1.4306 | 1 | 50 | 0.3 | 0.25 | Chevron | 3.7 |
| EN AW-7075 | 1 | 50 | 0.2 | 0.25 | Chevron | 2.7 |

[a] width, [b] thickness, [c] notch length, [d] maximal load in a cycle

To enhance crack-tip visibility for VIM, a mirror-like finish was produced on the specimen surfaces. A polished band, $0.8\ to\ 1.2\ mm$ wide, was maintained along the expected crack growth path, while the remaining area was coated with matte white paint and then partly covered with black paint to create the speckle pattern for DIC measurement (Fig. 2). This novel sample preparation [10] allowed for the use of both VIM and DIC on the same side of the sample, effectively eliminating the influence of non-uniform crack growth across the sample thickness from the validation.

The mirror-like finish and preservation of the unspeckled band on the polished surface were implemented solely to facilitate validation and benchmark comparison; they are not required in the final methodology, which is designed to operate with a speckle pattern covering the entire region of interest (ROI).

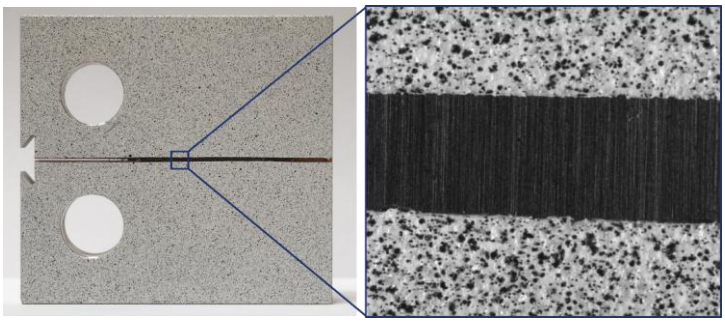

*Fig. 2: CT sample with applied DIC speckle pattern (left) and the detail of the polished band and the speckles (right) [10]*

### 4.1.2 Experimental Setup

The fatigue tests were carried out using an Amsler 20 HFP 5100 resonant pulsator machine. Images were captured with a FLIR 8.9-megapixel global shutter camera, equipped with a TC3MHR016-C telecentric lens (Fig. 3) at a magnification of 0.85 providing a viewing area of approximately $16.7 \times 8.8\ mm$.

To compensate for the low lens speed and the short exposure time (0.5 ms), used to prevent motion blur, two 50 W LED lights were positioned close to the sample to provide adequate illumination. The camera was mounted on a slider for precise focus adjustment.

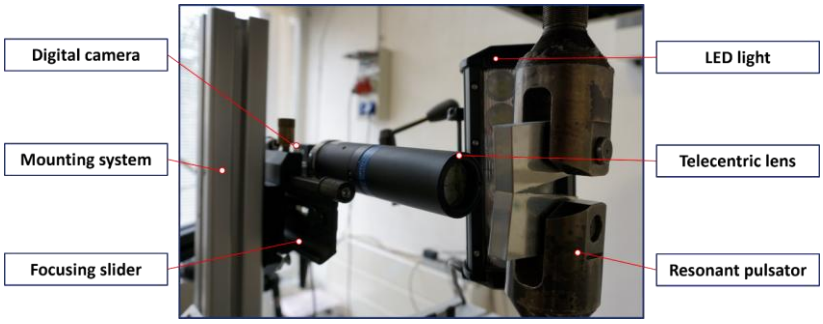


*Fig. 3: Detail of the optical system in front of the testing machine [10]*

### 4.1.3 Testing Procedure

The cycle parameters were set for a stress ratio $R = 0.1$ and the load levels used are detailed in Tab. 1.

Throughout the experiment, the test was periodically halted (readout) at various crack lengths to gather high-quality images for the VIM. These images also formed the static dataset for the IPM (IPMs) and DTM. The stopping intervals were based on previous crack length increments to achieve the most uniform distribution of crack lengths. To enhance the visibility of the crack tip, an overload of approximately 33% (assessed empirically) above the maximum cyclic load ($P_{max}$) was applied during the readout (Fig. 4). This approach was required to ensure a level of crack visibility similar to what is provided by a standard traveling microscope, which usually targets a much smaller region close to the crack tip.

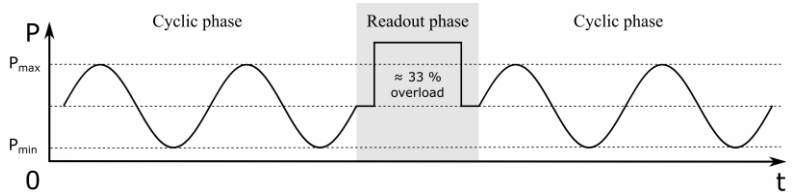


*Fig. 4: Scheme of the testing procedure, including periodic halting (readout) between cyclic phases and application of overload during the readout [10]*

Since the objective was to compare measured crack lengths between methods rather than to investigate FCGR, this overload did not adversely affect the results. The readout phase is not part of the proposed methodology and was introduced only for purposes of IPM development and validation.

### 4.1.4 Data Acquisition during Ongoing Tests

To assess the feasibility of the crack length measurement without stopping the experiment, a synchronization device monitored the force readings from the testing machine [10] and sent a trigger to the camera at the moment of maximum force (when the crack was most open) to capture an image after skipping $n_{sync}$ cycles, as schematically depicted in Fig. 16.

Subsequently, this approach was used to identify the first image after the ramp-up phase of the test following each readout. These images were used to construct the dynamic dataset (IPMd), ensuring a representative comparison to the baseline, assuming that the crack did not grow—or grew only negligibly—during the ramp-up. The dynamic dataset was then used to assess the IPM performance during the ongoing experiment.

## 4.2 Methods

The coordinate system, which will be used throughout the following sections is defined in Fig. 6.

### 4.2.1 Visual Inspection Baseline

To assess the crack length using VIM, it was necessary to identify crack tip locations (Fig. 5).

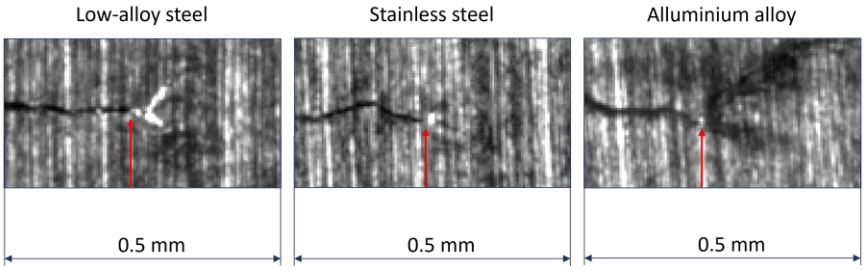


*Fig. 5: Examples of the area around the crack tip (red mark) for each material [10]*

The resolution of the imaging system is inherently limited by diffraction and system imperfections, resulting in some blurring of the crack tip; therefore, the crack-tip coordinate—and thus the baseline crack length ($a_b$) was expressed as the interval $a_b = a_{bm} \pm \delta_{cl}$ [10], where $\delta_{cl}$ represents the crack length assessment error and $a_{bm}$ is the ***midpoint*** of the estimated readout-error interval. The error distribution was positively skewed, and no general dependence on crack length was observed. Tab. 2 provides a summary of the crack length assessment errors.

*Tab. 2: Summary of crack length assessment errors ($\delta_{cl}$) – for readability converted from mm to µm [10]*

| *Material* | *Piece No.* | *min* $\delta_{cl}$ $[\mu m]$ | *mean* $\delta_{cl}$ $[\mu m]$ | *std* $\delta_{cl}$ $[\mu m]$ | *max* $\delta_{cl}$ $[\mu m]$ |
|---|---|---|---|---|---|
| 38MnVS6 | 1 | 5.5 | 14.5 | 6.0 | 29.0 |
| 38MnVS6 | 2 | 5.0 | 14.0 | 5.5 | 28.0 |
| 1.4306 | 1 | 4.0 | 14.5 | 5.5 | 22.5 |
| 1.4306 | 2 | 6.0 | 14.0 | 6.0 | 24.0 |
| 1.4306 | 3 | 8.5 | 16.5 | 5.0 | 24.0 |
| EN AW-7075 | 2 | 8.5 | 16.5 | 4.5 | 21.5 |

### 4.2.2 Image Processing and Data Extraction

To implement the DTM and IPM, deformations were extracted from the available images using DIC. For this task, the commercial software Alpha DIC from X-Sight was utilized. Within the software, a series of line segments perpendicular to the crack path served as virtual extensometers (VEs) (Fig. 6). In the following text, $n_{ve}$ indicates their number, $l_{ve}$ their length and $w_{ve}$ the length of the window they cover. Their displacements between consecutive images were monitored by the DIC algorithm with subpixel resolution.

The choice of $l_{ve,d}$ ensured that the entire correlation subset (also referred to as the subset or template) lay on the speckle pattern as close to the polished band as possible. Subset dimensions are a key factor in the quality of DIC results; therefore, they were studied in the following sensitivity analysis.

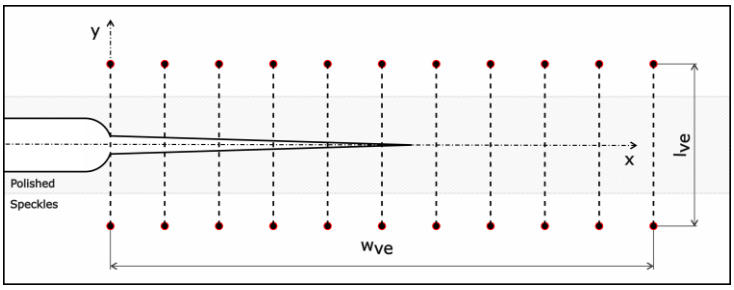


*Fig. 6: Schematic illustration of the VEs (virtual extensometers) placement in the current experimental program, showing the defined variables used in the IPM (Inflection point method) [10]*

### 4.2.3 Strain Threshold Method as the Benchmark

Building upon the deformation data extracted from DIC, the DTM was implemented to serve as the benchmark representing the currently used 1D DIC evaluation approach for the comparison with the proposed IPM, specifically its strain-based variant (STM).

The primary difficulty in applying the STM lies in accurately determining the threshold value $\varepsilon_{th}$. Since determining $\varepsilon_{th}$ is beyond the scope of this work, it was chosen based on VIM results, ensuring optimal STM performance for each dataset.

In selecting these values, a significant limitation was identified: a constant threshold cannot accurately estimate crack lengths across a wide range. This limitation is illustrated in Fig. 7, which shows results from applying three different threshold values.

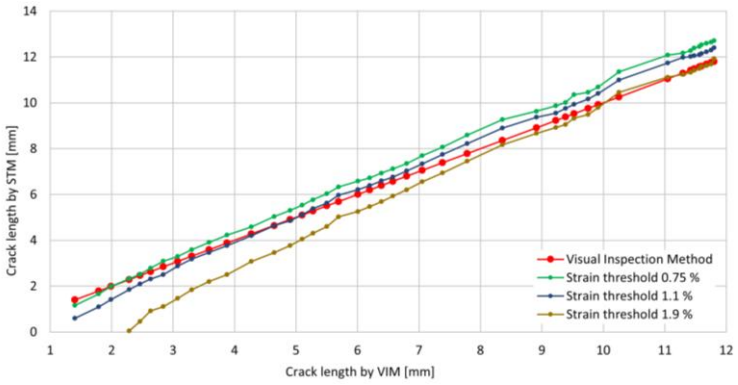


*Fig. 7: STM (Strain threshold method) results for three different threshold values compared with VIM (Visual inspection method) results for low-alloy steel sample No. 1*

## 4.3. Inflection Point Method

The datasets generated by DIC, which are used as inputs to IPM, are referred to as COD projection (CODP) curves. To create the CODP curve, the change in the length of each VE was plotted as a function of its distance from the notch. These curves qualitatively represent the crack opening displacement along the crack faces, though they are not quantitatively identical since they are measured at some distance from the faces.

This is particularly problematic around the IP, where the expected behaviors $r^{\frac{3}{2}}, \theta = \pi\, rad$ (process zone) and $r^{\frac{1}{2}}, \theta = \pi\, rad$ (outside the process zone) [22], are not followed, and the curve is noisy. Therefore, Gaussian-process regression (GPR) was chosen to identify the IP location. GPR also enables adaptation to changing conditions, learning online during the test.

The algorithm itself consists of three phases. In Phase 1 (P1), the entire CODP curve is fitted by GPR to estimate the IP location. In Phase 2 (P2), the fitting is performed locally around the P1 estimate, using 40% of $w_{ve}$, since P1 did not locate the actual inflection point accurately (Fig. 8). Therefore, the predicted locations from P2 were preferred over those from P1.

Additional corrective steps and conditions were applied to increase the robustness of the algorithm. For example:

- For shorter cracks ($a < 2.5\,mm$) the fitting interval ***was made*** asymmetric around the P1 IP, which helped achieve good localization for $a > 1.5\,mm$, which is the limiting lower bound for IPM use.
- If the local fit in P2 did not have the correct shape (e.g., two inflection points, especially for long cracks), the P2 interval was reduced to 20% of $w_{ve}$ and P2 was repeated.
- If that did not help, the P1 inflection point was taken as the crack tip.

Since GPR requires points on both sides of the IP, the upper bound $a < (w_{ve} - 0.5)\,mm$ was identified, ***beyond which*** the method does not perform well. Finally, the crack tip position was used as the final crack length, $a_{IPM,i}$.

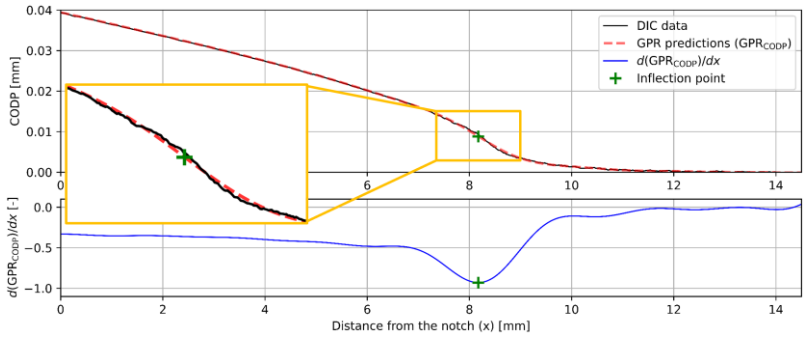


*Fig. 8: Example of data from DIC and Gaussian process regression (GPR) global predictions; localization of the IP (inflection point) using the first derivative of GPR (bottom); detail of the sharp transition around the IP (left), which is not properly captured by phase 1 of GPR; for EN AW-7075 sample [10]*

## 4.4. Sensitivity Analysis

This section examines how various parameters influence the performance and robustness of the IPM. The analysis is organized into three parts: variables related to image processing, parameters within the IPM algorithm, and test variables. Mean Absolute Error (MAE), Root Mean Square Error (RMSE), and Mean Absolute Percentage Error (MAPE) [25], quantify deviation from VIM baseline. Additionally, an overall loss function $\mathcal{L}$ was defined as the average of MAE, RMSE and MAPE; for reporting, values were normalized to the final IPM settings.

### 4.4.2 DIC-Related Parameters

The parameters related to image correlation, specifically $l_{ve}$, correlation subset-size, and $n_{ve}$ were evaluated. Fig. 9 shows $l_{ve}$ to be a very influential parameter requiring further attention (addressed later). The impact of subset size is illustrated in Fig. 10, which shows good performance in all cases except when the subset is very small**.** The best results were achieved with a narrower subset along the crack path and a larger one perpendicular to it, specifically $(w_{sub}, h_{sub}) = (21, 81)\,px$.

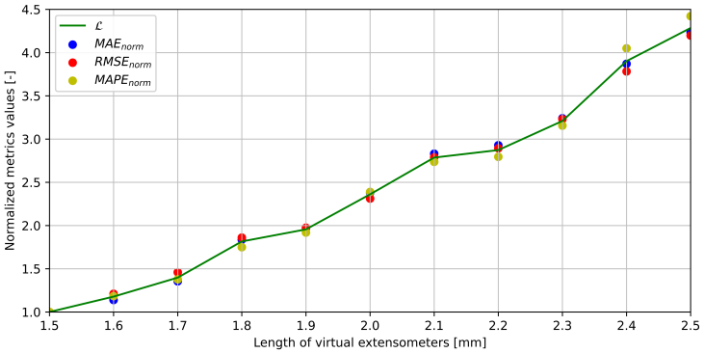


*Fig. 9: Relationship between normalized metrics values and length of virtual extensometers ($l_{ve}$) for all static datasets [10]*

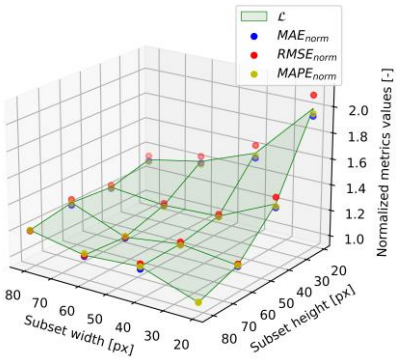


*Fig. 10: Analysis of subset dimensions $(w_{sub}, h_{sub})$ [10]*

From the study of $n_{ve}$, user recommendations were formulated as $w_{ve,r} \in \langle 10.0, 14.5 \rangle\,mm$ and VE spatial frequency $f_{ve,r} \in \langle 11, 14 \rangle\,mm^{-1}$. Multiplying values from these intervals yields $n_{ve}$ for which the method produced satisfactory results.

### 4.4.3 IPM-Related Parameters

The internal IPM parameters, which are not user-exposed, were studied to find optimal preset values that perform well within regions where the method is relatively insensitive to parameter choice. The studied factors included, for example, the criterion deciding when P1 is favored over P2, the size of the P2 interval, and the amount of its reduction for a second fitting.

### 4.4.4 Test-Related Parameters

To further evaluate the impact of load levels, an additional procedure was included for the EN AW-7075 No. 2 sample. During several readings, the static load was gradually increased in five consecutive steps up to 5 $kN$. This created four sets of load-dependence curves at constant crack lengths.

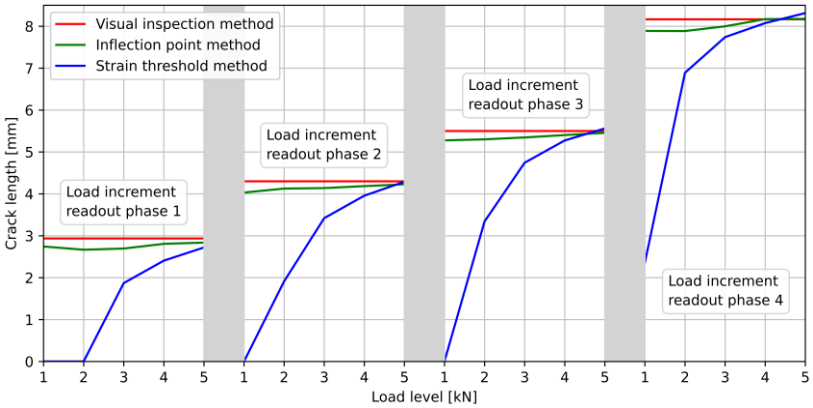


*Fig. 11: Results of the methods comparison in terms of load dependency for the four different load increment readout phases during the aluminum alloy No. 2 sample testing [10]*

While the IPM results do show some dependence on the load levels, this dependence is much less pronounced than that of the STM (Fig. 11). For example, at a crack length of 5.5 mm and an load level of 1 $kN$, STM estimates no crack, whereas IPM provides 5.28 mm—demonstrating significantly greater robustness and versatility.

Regarding different materials or specimen sizes, no dependence was detected, as shown in the next section.

## 4.5 Results – Validation and Comparison

The method-comparison results are expressed in the form of deviations from the baseline crack length ($\Gamma_{bm,i}$, $\Gamma_{IPMs,i}$, $\Gamma_{IPMd,i}$, $\Gamma_{STM,i}$) as a function of the baseline crack length $a_{bm}$ for each CT sample. These correspond to the results obtained from VIM, the IPMs, IPMd, and the STM applied to the static dataset, respectively. The values are defined as [10]:

$$\Gamma_{j,i} = a_{j,i} - a_{bm,i};\ j \in \{bm, IPMs, IPMd, STM\} \quad (1)$$

Additionally, the band $\pm\delta_{cl,i}$ is plotted along with $\Gamma_{bm,i}$ values. This plotting highlights differences between methods that would be less apparent if crack lengths were plotted directly on the y-axis. For the x-axis, using cycle count would yield uneven spacing (more cycles between readouts for shorter cracks); using baseline crack length spaces points more evenly and clarifies trends.

$$\Gamma_{j,i} = a_{j,i} - a_{bm,i};\ j \in \{bm, IPMs, IPMd, STM\} \quad (1)$$

*Tab. 3: Summary of overall results for particular methods [10]*

| | $MAE$ [$\mu m$] | $RMSE$ [$\mu m$] | $MAPE$ [%] | $\mathcal{L}$ [−] |
|---|---|---|---|---|
| IPMs | 24 | 31 | 0.50 | 1.0 |
| IPMd | 54 | 77 | 1.15 | 2.3 |
| STM | 215 | 274 | 5.43 | 10.8 |

Fig. 12, Fig. 13 and Fig. 14 present method comparisons for low-alloy steel, stainless steel, and aluminum alloy,

respectively. In each figure, the STM curves are most prominent, exhibiting an approximately linear trend in deviation from the correct values. This reflects the crack-length dependence of STM results (see section 4.2.3.)

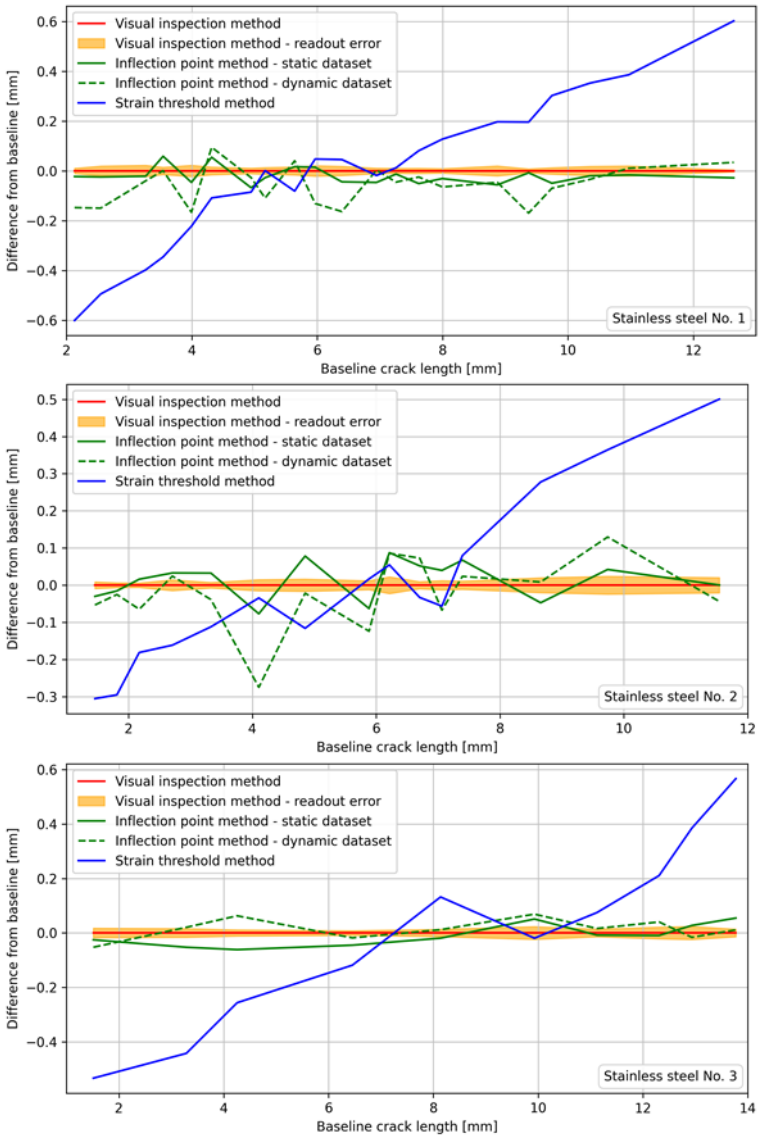


*Fig. 12: Methods comparison in terms of their differences from the baseline as a function of baseline crack length for the stainless-steel sample No.1, No.2 and No.3*

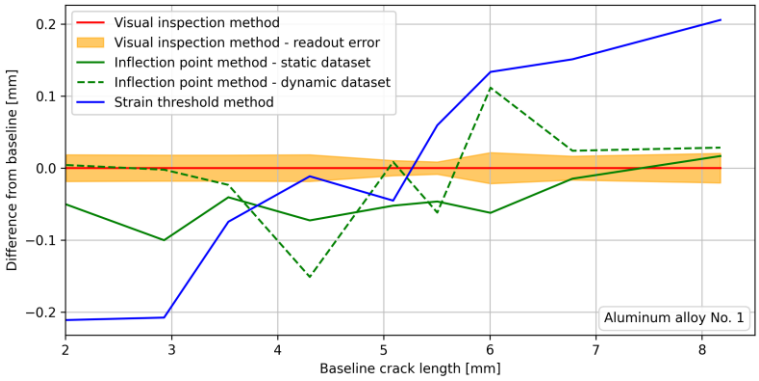


*Fig. 13: Methods comparison in terms of their differences from the baseline as a function of baseline crack length for the aluminum alloy sample No.2 [10]*

On the other hand, the proposed method does not systematically deviate from the baseline but fluctuates around

it. When IPM is applied to the dynamic dataset, more outliers appear; however, the overall results are still acceptable. Tab. 3 summarizes the overall results and highlights key performance metrics.

In summary, IPM yields results that closely match the baseline for both static and dynamic datasets, although its accuracy is about 2.3 times lower for the dynamic dataset than for the static one. In comparison, STM accuracy for the static dataset is approximately 10.8 times worse than that of IPM.

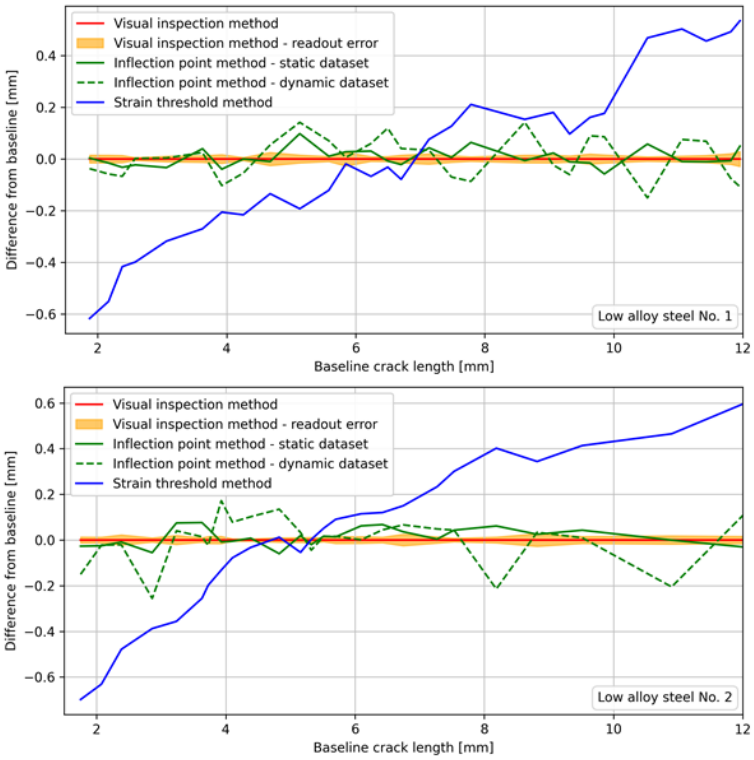


*Fig. 14: Methods comparison in terms of their differences from the baseline as a function of baseline crack length for the low-alloy steel sample No.1 (top) and No.2 (bottom) [10]*

## 4.5 Processing scheme optimization

The initial IPM implementation was computationally demanding, with the most demanding part being GPR fitting on the entire CODP curve. Thus, the IPM processing scheme was refactored to achieve efficient computation while preserving accuracy, reducing computational time by ~55%. This version is called fIPM (fast IPM).

The key assumption behind this optimization is that the crack propagates gradually during FCGR testing and relatively slowly with respect to acquisition speed, so there is little change between consecutive images.

The most significant change is the substantial reduction in Phase 1 (P1), which involved the largest number of points in the GPR regression and thus dominated runtime. Nevertheless, P1 still plays a vital role, as it is performed with a defined frequency and under defined conditions to correct the P2 result should it produce an outlier. Accordingly, the P1 IP estimate was replaced by the P2 IP from the previous iteration.

## 4.6 Discussion

The IPM and the inflection-point principle were successfully validated on a static dataset, as their results align well with the baseline. Furthermore, the practicality of measuring and implementing the proposed method in a real-time experiment (dynamic dataset) was demonstrated. While IPM shows lower accuracy on the dynamic dataset, the outcomes are still valid.

IPM has demonstrated robustness and adaptability to test variables, especially changes in load levels—a significant advantage over STM—as evidenced by the sensitivity analysis. No effect of sample size (constraint) or material was detected, as results did not change with these factors.

At present, IPM is recommended only for metallic materials, since the inflection-point principle has not yet been validated for other materials such as composites or plastics—an area for future research. The method's validation

on another specimen type (MT) is demonstrated in the following chapter.

Regarding DIC-setup parameters, $l_{ve}$ has a significant impact on IPM results. Current findings indicate that shorter lengths are more favorable, though values smaller than 1.5 mm could not be tested due to the polished validation band. Smaller values may enhance accuracy, provided the propagating crack remains outside the correlation-subset areas throughout the experiment; this assumption is examined in the following chapter. For other user settings, recommendations are given in section 4.4.2 (DIC-Related Parameters), and the limitations can be summarized as $1.5\ mm < a < (w_{ve} - 0.5)\ mm$.

Finally, the limitation of the method *for real-time measurement* was tested and compared with STM and full-field DIC. For full-field DIC, it was assumed that a region of $l_{ve} \times w_{ve}$ was covered by a uniform mesh of equilateral triangles, with side length equal the distance between neighboring VEs.

*Tab. 4: IPM algorithm with improved computational efficiency (fIPM) in comparison with STM and full-field DIC*

| | fIPM | STM | Full-field DIC |
|---|---|---|---|
| Hardware operations[a] [ms] | 15 | 15 | 15 |
| Data extraction from image (DIC)[b] [ms] | 34 | 34 | 550 |
| Crack length evaluation [ms] | 32 | 1.4 | N/A |
| **Max. achievable frame rate[c]** [$s^{-1}$] | **20.4** | **20.4** | **1.8[d]** |

[a] using parallelized computation on four cores of an AMD Ryzen 9 5950X at 4.2 GHz

[b] using serial computation on one core at 4.2 GHz

[c] Considering the *processing sequence*, where the computations related to crack length assessment for current iteration run in parallel with the image acquisition and DIC data extraction in the following iteration. The frame rate is calculated as *1000 ms / max(Hardware operations + Data extraction from image (DIC), Crack length evaluation);* unit is equivalent to FPS.

[d] Assuming that *crack length evaluation < (Hardware operations + Data extraction from image (DIC))*

# 5 Fatigue Crack Growth Rate Validation Analysis

To further assess IPM—specifically fIPMf—this chapter validates crack length estimates via FCGR during running fatigue tests.

A head-to-head comparison with STM in Chapter 4 showed that STM requires dataset-specific thresholds, is strongly load-dependent, and yields higher errors than IPM at similar throughput. Accordingly, Chapter 5 omits STM and focuses on validating fIPMf against the non-DIC baseline (VIM) and quantifies FCGR accuracy under uninterrupted testing.

## 5.1 Experimental Program for Data Acquisition

The experimental program (*current EP)* closely follows section 4.1 (*previous EP*). Differences are noted below.

Two MT samples, prepared in accordance with ASTM E647 [3], were used in this study. The samples are designated as MT No. 2 and MT No. 4. Both samples were made from the same material—standard non-alloy structural steel 1.0038 (S235JR)—and had identical dimensions $W = 60\,mm$ and $B = 6\,mm$. Slot notches $a_{n,MT2} = 5.05\,mm$ and $a_{n,MT4} = 5.06\,mm$ were machined to emanate from a central hole. A clamping device was used instead of bolted grips. The speckle pattern was applied over the entire ROI, as shown in Fig. 15.

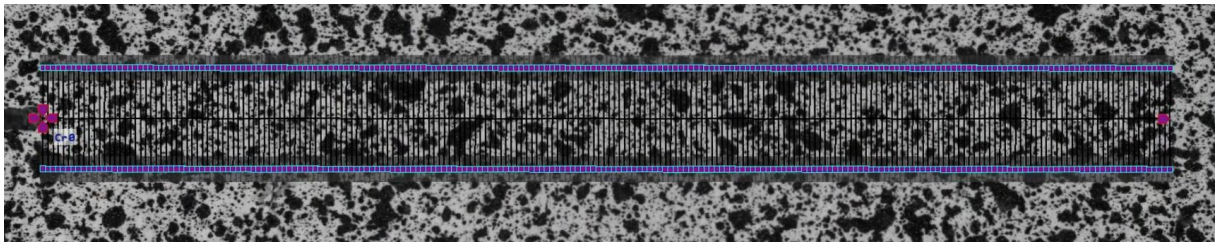

*Fig. 15: Speckle pattern on the surface of the MT No. 4 sample, with 200 virtual extensometers (VEs) placed along the measurement line. The distance from the first VE (located at the notch tip on the left) to the last on the right is 14.5 mm.*

Tests used a 60 $kN$ Schenck PVQ resonant pulsator. Optics and other components matched the previous EP (Fig. 3). The experiment ran continuously except during load changes; images were acquired every $n_{sync}$ cycles as in Fig. 16.

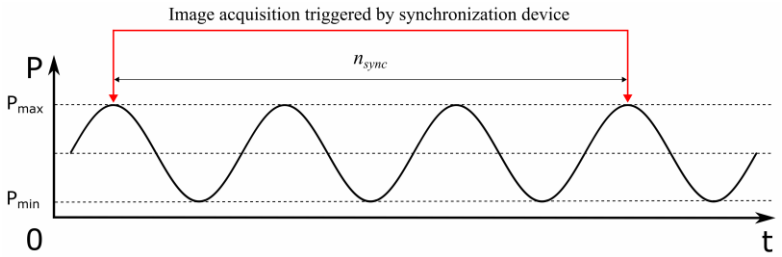


*Fig. 16: Schematic of the testing procedure utilizing a synchronization device to trigger image acquisition every $n_{sync}$ cycles, at the moment when the crack is most open (the loading cycle is at its maximum force phase)*

For MT No. 2, a *K*-decreasing test with stepped force shedding was run at $R = 0.1$. Force amplitudes are summarized in Tab. 5 along with the corresponding $n_{sync}$ values.

*Tab. 5: Force amplitudes ($P_a$) and $n_{sync}$ parameter for each dataset collected on the MT No. 2 sample.*

| *Dataset No.* | $P_a$ *[kN]* | $n_{sync}$ $[-]$ | *Dataset No.* | $P_a$ *[kN]* | $n_{sync}$ $[-]$ |
|---|---|---|---|---|---|
| 0 | 14.0 | 70 | 5 | 7.5 | 50 |
| 1 | 12.0 | 70 | 6 | 6.9 | 50 |
| 2 | 10.0 | 60 | 7 | 6.5 | 50 |
| 3 | 9.0 | 50 | 8 | 6.2 | 50 |
| 4 | 8.5 | 50 | | | |

Note on deviations from ASTM E647 [3]:

- Change in $P_{max}$ sometimes exceeded the recommended 10% (notably the first two steps).
- After each change, $\Delta a$ used for evaluation was below the recommended $\Delta a_{KD,r} \geq 0.5\ mm$.
- Evaluation used a single measured crack size rather than the recommended average of four.

MT No. 4 was tested *K*-increasing at constant $P_a = 11\ kN$ and $R = 0.1$, so crack extension increased $\Delta K$ and thus FCGR. Only post-ramp-up data were evaluated.

## 5.2 Data Processing and Filtering Implementation

DIC settings matched the previous EP, except $l_{ve}$ was swept $0.5 - 1.5\ mm$ (step 0.1 mm) to study the effect of VEs' length, previously identified as a highly influential parameter.

As load decreased (MT No. 2, datasets 0→8), CODP amplitude shrank and noise in successive crack-length values rose, as demonstrated in Tab. 6 (the maximum displacement at the crack tip in dataset 8 is almost nine times smaller than for dataset 0) and in Fig. 17 (load-noise dependence). This motivated temporal filtering in fIPM.

*Tab. 6: Examples of DIC-measured displacement values, for selected datasets and locations ($l_{ve} = 1.3\ mm$)*

| Sample, dataset | *Location* | *Max. CODP*[a] $[\mu m]$ |
|---|---|---|
| MT No. 2, Dataset 0 | Notch tip | 11.9 |
| | Crack tip | 5.3 |
| MT No. 2, Dataset 8 | Notch tip | 3.2 |
| | Crack tip | 0.6 |

[a] from the end of the dataset

A Kalman filter (KF) was adopted because it filters in real time without requiring future data. A fixed-parameter KF proved insufficient across the force range, so an adaptive variant was used, learning process/measurement noise online. As a final enhancement, a soft-monotonicity safeguard (non-decreasing crack length with outlier tolerance) was added. The final pipeline with KF is called fIPMf (fast Inflection point method filtered).

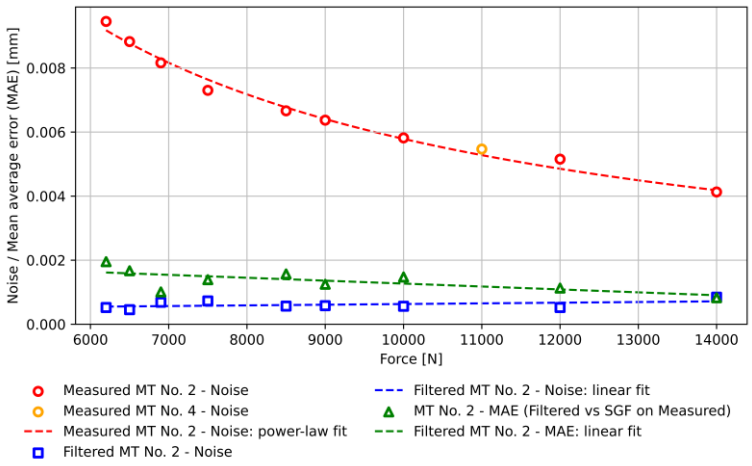


*Fig. 17: Load–noise dependence for both measured and filtered data, together with load–MAE (mean absolute error) dependence for the filtered data, where the MAE is calculated with respect to the smoothed reference curve obtained from measured data. Virtual extensometers' length $l_{ve,d} = 1.5\ mm$*

The filtering effectiveness was assessed by comparing noise levels with a smooth reference curve obtained with a Savitzky-Golay filter (SGF) in post-processing. Noise was quantified as the standard deviation of the residuals, calculated as the difference between the evaluated crack length series (raw or filtered) and its SGF-based reference (Fig. 17). KF reduced noise by approximately one order of magnitude to $< 1\ \mu m$ across all load levels.

The mean absolute error (MAE) of the filtered crack length signal was computed as the average of absolute difference between the fIPMf series and SGF-smoothed reference curve derived directly from the measured data. The results indicate an average deviation of $1 - 2\ \mu m$ caused mainly by the soft-monotonicity condition.

## 5.3 Validation of Measurement and Method

While validating fIPMf for crack-length and FCGR during running tests, the same datasets were used to assess the effect of VEs' length. Consequently, the presentation of the validation and parameter study results is interlinked.

### 5.3.1 Baseline Data (VIM Tests)

The baseline validation data were kindly provided by the Institute of Physics of Materials in Brno and are used here with permission. These measurements were obtained using VIM on samples of the same geometry and material, tested on the same machine as in section 6.1. The specimens were designated MT No. 1–4; notably, MT No. 2 and MT No. 4 were later used for fIPMf validation in this chapter. A NASGRO fit based on the following equation ([26], [27]):

$$\left(\frac{da}{dN}\right)_{NG} = C_{PL}\Delta K_{eff}^{m_{PL}}\left[1-\frac{\Delta K_{th}}{\Delta K}\right]^{p_{NG}}\left[1-\frac{K_{max}}{K_c}\right]^{-q_{NG}} \qquad (2)$$

was provided together with the measured points. The equation can be reduced to Paris law (given later as equation (5)), thus the coefficients $C_{PL}$ and $m_{PL}$ are used for comparison in the next chapter. For definitions of the remaining quantities and parameters, see the cited sources.

An overview of the tests appears in Tab. 7. All tests were *K*-decreasing except for MT No. 3, which included a subsequent *K*-increasing phase. The stress ratio was $R = 0.1$ in all cases, matching the fIPMf measurements.

FCGR was evaluated using the average crack size over four measurements (front/back on two cracks). Consecutive changes in $P_{max}$ stayed below 10% (modus ≈ 2.5%). After each $P_{max}$ reduction, $\Delta a$ remained consistently below the recommended $\Delta a_{KD,r} > 0.5\ mm$.

*Tab. 7: Overview of MT No. 1–4 tests performed using VIM (Visual inspection method), ($R = 0.1$)*

| *MT No.* | $P_a$ [a] $[kN]$ | $K_{max}$ [b] $[MPa\sqrt{m}]$ | $\frac{da}{dN}$ [c] $\left[\frac{mm}{cycle}\right]$ | $N_{overall}$ [d] $[10^3]$ | *Points* [e] $[-]$ |
|---|---|---|---|---|---|
| 1 | $\langle 11.70 - 8.21\rangle$ | $\langle 9.75 - 7.85\rangle$ | $\langle 1.70\times10^{-6} - 1.67\times10^{-8}\rangle$ | 1968 | 12 |
| 2 | $\langle 11.70 - 5.76\rangle$ | $\langle 9.17 - 6.02\rangle$ | $\langle 1.63\times10^{-6} - 2.50\times10^{-10}\rangle$ | 5189 | 21 |
| 3 | $\langle 13.63 - 6.06\rangle$, 9.00 | $\langle 11.97 - 6.47\rangle$, $\langle 9.10 - 17.29\rangle$ | $\langle 5.97\times10^{-6} - 5.00\times10^{-9}\rangle$, $\langle 6.25\times10^{-7} - 3.73\times10^{-5}\rangle$ | 4853, 2040 | 18, 34 |
| 4 | $\langle 13.63 - 6.54\rangle$ | $\langle 11.22 - 6.88\rangle$ | $\langle 4.40\times10^{-6} - 3.75\times10^{-9}\rangle$ | 5132 | 19 |

[a] cycle force amplitude; [b] cycle maximum stress intensity factor; [c] fatigue crack growth rate; [d] overall number of cycles achieved in test; [e] in the $da/dN = f(K_{max})$ plot

### 5.3.2 Evaluation of MT Samples Using fIPMf

For MT No. 2 (Fig. 18), each dataset yields one point in the $da/dN - K_{max}(a)$ plot.

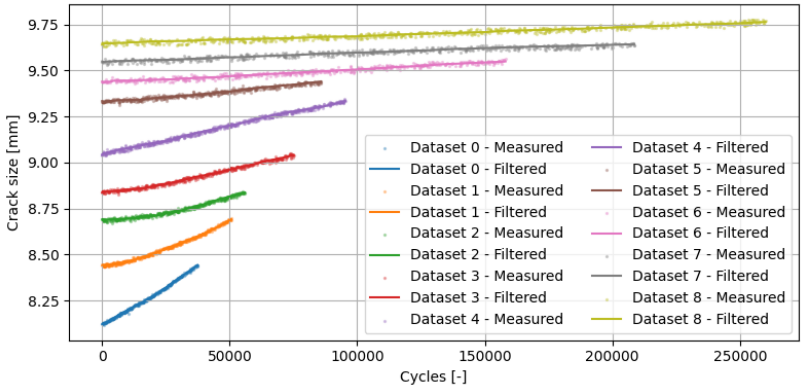


*Fig. 18: MT No. 2 datasets No. 0–8 with measured and filtered crack size values obtained at virtual extensometers' length $l_{ve} = 1.3\ mm$. The vertical axis represents crack size (crack-length value from fIPM/fIPMf + corresponding notch length).*

The FCGR for a particular dataset was evaluated as:

$$\left(\frac{da}{dN}\right)_{fIPMf} = \frac{a_{fIPMf}(N_{end}) - a_{fIPMf}(N_{start})}{N_{start}} \tag{3}$$

and the corresponding maximum SIF as:

$$K_{max} = (1-R)^{-1}\Delta K_{MT}(a_{mid}) \tag{4}$$

where $\Delta K_{MT}$ is the SIF range for the MT specimen as defined in [3] and $a_{mid}$ is the crack size (fIPMf prediction + notch length) at the midpoint of the evaluation interval, which, in this case, spans the entire dataset.

For MT No. 4, larger crack extension allowed multiple points per dataset. Extraction intervals were $\Delta a_{FCGR}^{thr} = 0.4\,mm$. Additionally, only intervals with $N < 450000$ were retained to ensure comparability across all $l_{ve}$ values. As shown in Fig. 19, later data exhibited reduced FCGR and maximum crack size due to a slight crack-path deviation, which caused surface discontinuities to interfere with the correlation subsets at the VE endpoints (see section 4.6).

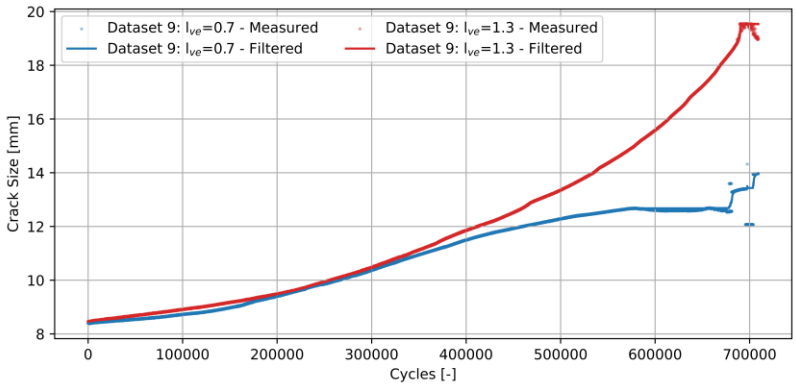


*Fig. 19: Measured and filtered crack size values for the MT No. 4. The vertical axis represents crack size (crack-length value from fIPM/fIPMf + corresponding notch length).*

### 5.3.3 Influence of Virtual Extensometers' Length and Error Analysis

For MT No. 2, which covers a wide range of applied loads, $l_{ve}$ had little effect on datasets 0–5. However, at lower loads (datasets 6–8), FCGR values exhibited an increasing trend toward smaller $l_{ve}$.

Next, the $K_{max}$ vs. $l_{ve}$ relation was assessed. For higher-load datasets (0–5), $K_{max}$ decreased gradually from $l_{ve} = 1.5\,mm$, with the decline becoming more pronounced for $l_{ve} < 1\,mm$. This suggests that lowering $l_{ve}$ leads to a systematic reduction in the predicted crack length at higher loads, while FCGR stayed constant. For datasets 6–8, a slight increase in $K_{max}$ was observed at smaller $l_{ve}$.

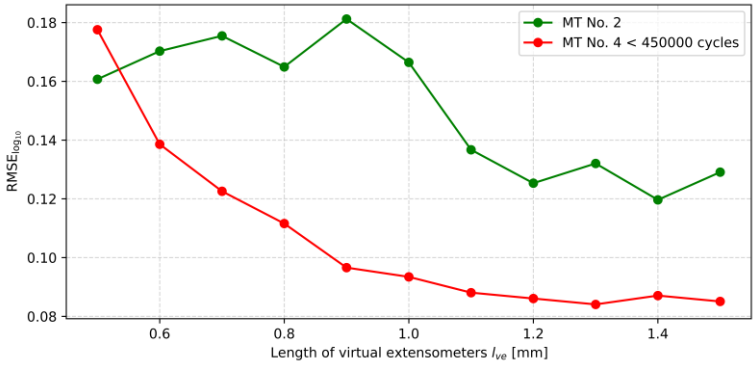


*Fig. 20: Comparison of fIPMf (fast Inflection point method filtered) crack growth rates with values predicted by the NASGRO equation from baseline data, for various virtual extensometers' lengths.*

All $da/dN - K_{max}(a)$ points (MT No. 2 and 4) were compared with the NASGRO baseline using RMSE in $log_{10}$ coordinates. Results (Fig. 20) show that for MT No. 2, the error increased for $l_{ve} < 1.1\,mm$, mirroring the FCGR

increase in datasets 6–8. For MT No. 4, errors were smaller, likely due to larger $\Delta a$ used in the evaluation, but they increased steadily toward the smaller $l_{ve}$, reflecting the crack path deviation and subset interference as described in section 5.3.2.

Overall, the performance is very promising. The best error value corresponds to a deviation of approximately 21% from the baseline, while the worst indicates about 51%. However, qualitative comparison of the $da/dN - K_{max}(a)$ curves shows that for smaller $l_{ve}$ the results deviate from the expected linear shape quite noticeably, indicating that the measurement is not reliable.

Based on these findings, $l_{ve,r} = 1.3\ mm$ is recommended as the midpoint of the stable interval $1.1 \leq l_{ve} \leq 1.5$. The value was selected to reduce the risk of crack-subset interference. The quantitative overview of residual errors and approximate deviations, including the datasets obtained using VIM, is provided in Tab. 8. It shows fIPMf variability comparable to the VIM baseline.

*Tab. 8: Overview of $RMSE_{log_{10}}$(root mean square error) and deviations from baseline (NASGRO).*

| | *fIPMf* [a], $l_{ve} = 1.3\ mm$ [b] | | *VIM* [c] | | | |
|---|---|---|---|---|---|---|
| *MT No.* | *2* | *4* | *1* | *2* | *3* | *4* |
| $RMSE_{log_{10}}$ | *0.120* | *0.084* | *0.613* | *0.185* | *0.152* | *0.121* |
| *Deviation [%]* | ≅ 32 | ≅ 21 | ≅ 310 | ≅ 53 | ≅ 42 | ≅ 32 |

[a] fast Inflection point method filtered; [b] virtual extensometers' length; [c] Visual inspection method

Finally, data points for $l_{ve,r} = 1.3\ mm$ are plotted with the baseline and NASGRO predictions in Fig. 21. Crack closure was included in the NASGRO fit.

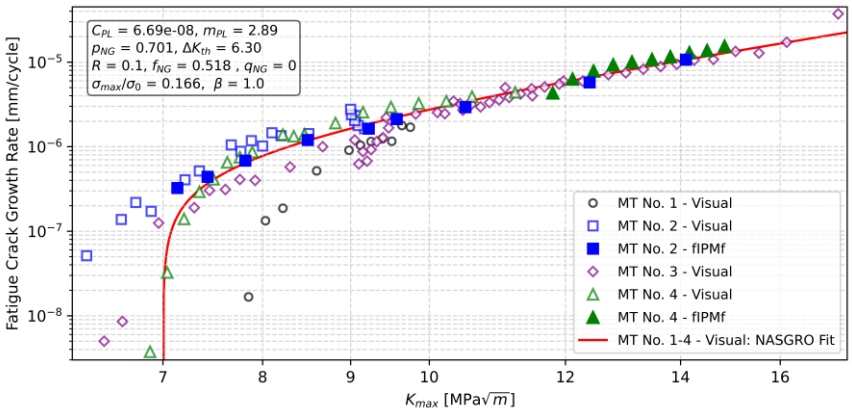


*Fig. 21: Raw baseline data measured with VIM (Visual inspection method) and tests evaluated by fIPMf (fast Inflection point method filtered), shown together with the NASGRO fit using all VIM datasets. Units: $C_{PL}$ $\left[mm\left(MPa\sqrt{m}\right)^{-m_{PL}}\right]$ for mm/cycle and for $\Delta K_{th}$ $\left[MPa\sqrt{m}\right]$.*

### 5.3.4 Conclusion

fIPMf provides reliable FCGR estimates during running tests, comparable to the established VIM baseline. Accuracy and robustness hold across a reasonably broad VE-length range, with larger deviations for excessively small $l_{ve,r}$ due to crack–subset interference. Within the recommended range, deviations from baseline remain acceptable, supporting application to uninterrupted testing.

# 6 Additional Measurements

To complement the previous fIPMf-based measurements performed on MT specimens, two additional CT specimens were tested and evaluated.

## 6.1 Experimental Program for Additional Data Acquisition

The experimental program for this chapter (*current EP)* closely follows section 6.1 (*previous EP*).

Two CT specimens prepared in accordance with [3] were used: S235(JR) and AISI 304L, hereafter abbreviated as CTCS and CTSS, respectively. Both specimens had identical dimensions $W = 50\,mm$ and $B = 10\,mm$. The corresponding notch lengths were: $a_{n,CTCS} = 12.62\,mm$ (straight-through) and $a_{n,CTSS} = 12.53\,mm$ (chevron). A speckle pattern was applied over the entire ROI.

Tests were performed on an Amsler 20 HFP 5100 resonant pulsator. Relative to the previous EP, a telecentric lens (WWK10-110-111) with a viewing area of approximately $14.1 \times 7.5\,mm$ was used. For both specimens, a *K*-increasing test was conducted with a single reduction in load. The stress ratio was $R = 0.1$ and the summary of the test is given in Tab. 9.

*Tab. 9: Overview of force amplitudes ($P_a$), $n_{sync}$, and the total number of cycles ($N_{overall}$) for each dataset collected on the CT S235 (CTCS) and CT AISI 304L (CTSS) samples*

| | $P_a\ [kN]$ | $N_{overall}\ [10^3]$ | $n_{sync}\ [-]$ |
|---|---|---|---|
| CTCS Dataset 0 | 3.25 | 260 | 100 |
| CTCS Dataset 1 | 2.75 | 134 | 100 |
| CTSS Dataset 0 | 3.25 | 89 | 50 |
| CTSS Dataset 1 | 2.75 | 87 | 50 |

Note on deviations from ASTM E647 [3]:

- Changes in $P_{max}$ between consecutive datasets exceeded the recommended 10%.
- A single measured crack size is used rather than the recommended average of two.

## 6.2 Data Processing

The DIC settings matched the previous EP, except that only the recommended $l_{ve,r} = 1.3\,mm$ was used. Crack lengths were extracted using the fIPMf method presented in Chapter 5. For SIF evaluation, the notch length was added to the measured crack lengths to obtain the crack sizes (see Fig. 22).

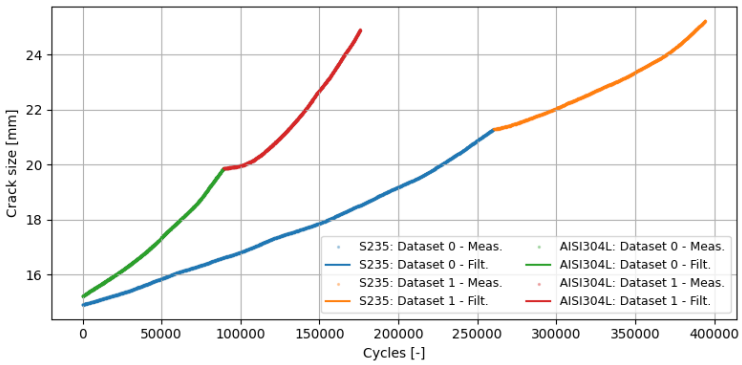


*Fig. 22: Measured and filtered crack size values for the CT specimens of S235 and AISI 304L over two consecutive datasets, with the load reduced in the second dataset. The vertical axis represents crack size (crack-length value from fIPMf + corresponding notch length).*

FCGR was evaluated according to equation (3); and $\Delta K_{CT}(a_{mid})$ was computed per from [3]. The evaluation interval length was $\Delta a_{FCGR}^{thr} = 0.25\,mm$. After the load reduction, the firt crack length increment of $\Delta a_{NE} = 0.5\,mm$ was excluded from the FCGR evaluation, consistent with $min(\Delta a_{KD,r})$ [3].

## 6.3 Results

The resulting data points of CTCS and CTSS are plotted in Fig. 23 for each specimen and dataset separately together with their Paris-law fits according to [27]:

$$(\mathrm{da/dN})_{PL} = C_{PL}\Delta K^{m_{PL}} \tag{5}$$

where $C_{PL}$ and $m_{PL}$ are Paris law coefficients.

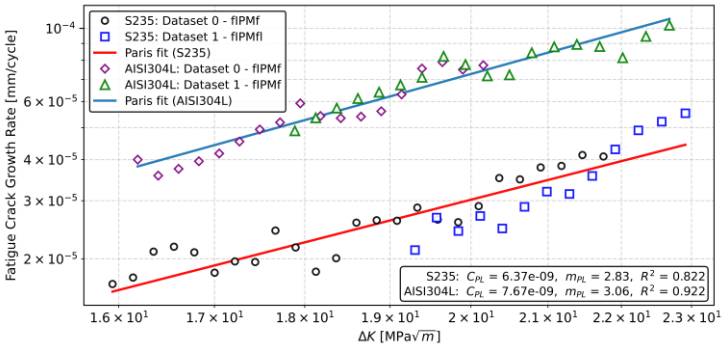


*Fig. 23: Data points from tests of CT specimens of S235 and AISI 304L evaluated using fIPMf (fast Inflection point method filtered), shown with the Paris law fit for each specimen separately.*

Because no same-specimen baseline was available, results were compared with literature values. Tab. 10 compares the Paris-law coefficients obtained for CTCS with published data for S235.

*Tab. 10. Input parameters (grey) together with the Paris-law coefficients $C_{PL}$ and $m_{PL}$, and the coefficient of determination $R^2$ for fatigue tests on S235 CT reported in the literature and obtained in this work (CTCS). Crack closure is not considered. Also the NASGRO fit on MT specimens is presented here without crack closure.*

| *Source* | $\{W, B\}$ $[mm]$ | $R$ $[-]$ | $C_{PL}\left[mm\left(MPa\sqrt{m}\right)^{-m_{PL}}\right]$ | $m_{PL}$ $[-]$ | $R^2$ $[-]$ |
|---|---|---|---|---|---|
| CTCS | {50,10} | 0.10 | $6.37 \times 10^{-9}$ | 2.83 | 0.822 |
| MT NASGRO (subsection 6.3.1) | {60,6} | 0.10 | $11.0 \times 10^{-9}$ | 2.89 | N/A |
| (2022, Comlekci et al.) [28][a] | {40,10} | 0.00 | $3.25 \times 10^{-8}$ | 2.53 | N/A |
| (2020, Seitl et al.) [29] | {50,10} | 0.10 | $2.00 \times 10^{-9}$ | 3.26 | 0.910 |

For CTCS, the Paris coefficients do not differ substantially from the literature, particularly for studies with the same thickness. They also align closely with the coefficients obtained in subsection 6.3.1 using the NASGRO equation on multiple MT datasets. Slightly higher values for the MT specimen can be attributed to its lower thickness (lower constraint), which tends to promote faster crack growth.

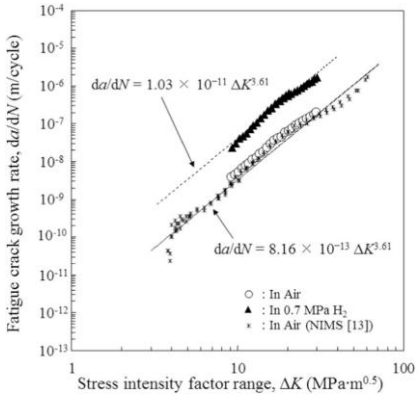


*Fig. 24: Fatigue crack growth rate plot [31] showing a steeper crack growth in the interval $\Delta K \in (10, \sim 18)\ MPa\sqrt{m}$ followed by a noticeably less steep slope in $\Delta K \in (\sim 18, 30)\ MPa\sqrt{m}$.*

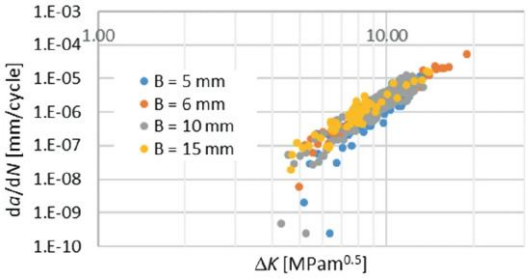


*Fig. 25: Fatigue crack growth rate plot for AISI 304L (1.4307, $B = 10\ mm$) [30] showing data in the interval $\Delta K = (\sim 4.5, \sim 10.5)\ MPa\sqrt{m}$, with many points near the $\Delta K_{th}$ indicating that they fall within a region where the Paris law does not apply.*

For CTSS, the Paris-law constants are listed in Tab. 11 together with literature values for AISI 304L under comparable conditions. Because the published studies do not always share the same $W$, $B$, and $R$, these parameters are reported for context. In this case, the crack-growth curve for CTSS is noticeably less steep than most literature datasets. When focusing on directly comparable conditions ($B = 10\,mm$ and $R = 0.1$), the discrepancy is pronounced, especially relative to [30].

*Tab. 11: Input parameters (grey) together with the Paris law coefficients $C_{PL}$ and $m_{PL}$ and the coefficient of determination $R^2$ for fatigue tests on CT samples from AISI 304L material found in literature and performed within this work (CTCS). The crack closure is not considered if not directly indicated. MT No. 2 and MT No. 4 are included to demonstrate the Paris law coefficients when the fit is performed in the near-threshold region.*

| *Source* | $\{W, B\}\ [mm]$ | $R\ [-]$ | $C_{PL}\left[mm(MPa\sqrt{m})^{-m_{PL}}\right]$ | $m_{PL}\ [-]$ | $R^2\ [-]$ |
|---|---|---|---|---|---|
| CTSS | {50,10} | 0.10 | $7.67 \times 10^{-9}$ | 3.06 | 0.922 |
| (2022, Seitl et al.) [30] (1.4306) | {50,10} | 0.1 | $3.00 \times 10^{-11}$ | 4.7 | 0.480 |
| (2022, Seitl et al.) [30] (1.4307) | {50,10} | 0.1 | $2.00 \times 10^{-11}$ | 4.98 | 0.650 |
| MT No. 2 and 4: Near threshold | {60,6} | 0.10 | $3.27 \times 10^{-11}$ | 5.07 | 0.988 |
| (2019, Nagaishi et al.) [31] | {51,10} | 0.1 | $8.16 \times 10^{-10}$ | 3.61 | N/A |

A closer inspection of the source curves shows that in [31] (where the discrepancy is smaller), the interval $\Delta K \in (10, \sim 18)\ MPa\sqrt{m}$ exhibits a steeper $da/dN - \Delta K$ slope than $\Delta K \in (\sim 18{,}30)\ MPa\sqrt{m}$ for *In Air* datasets (Fig. 24). The CTSS measurements correspond more to the latter interval, which helps explain the observed difference.

In the second study with comparable inputs [30], where the difference is larger, the $da/dN - \Delta K$ plot for 1.4307 (Fig. 25) uses $\Delta K \in (\sim 4.5, \sim 10.5)\ MPa\sqrt{m}$ (for $B = 10mm$). The very low FCGR near the lower bound suggests proximity to $\Delta K_{th}$, implying that a non-negligible portion of the data used for the Paris fit lies in the near-threshold Region I (see subsection 3.5.2), where the Paris law does not apply. A similar observation holds for 1.4306.

This remains a hypothesis, as the threshold value is not reported in the article. However, when near-threshold data are intentionally included in a Paris fit (see Fig. 26 for MT No. 2 and MT No. 4, where $\Delta K_{th}$ is known (subsection 6.3.1)), similarly high slope is obtained—even for a different material. Therefore, the results from [30] are not suitable for direct comparison with CTSS.

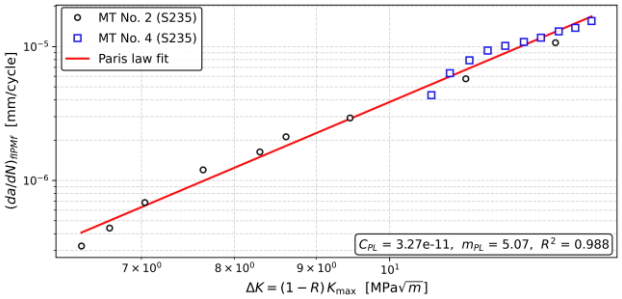


*Fig. 26: Example of a Paris-law fit to data in the near-threshold region where the Paris law does not apply.*

## 6.4 Conclusion

CTCS shows Paris-region behavior consistent with the literature and, more importantly, with the earlier NASGRO evaluation on MT datasets; modest differences likely reflect thickness-related constraint effects.

Conversely, CTSS is less steep than many published datasets under comparable conditions; thorough examination of the source data reveled, that differing ΔK windows and inclusion of near-threshold data likely those Paris fits, precluding direct comparison.

# 7. Methodology Summary & Implementation Guide

This chapter condenses the thesis into a deployable workflow for real-time crack length and fatigue crack growth rate (FCGR) assessment using digital image correlation (DIC).

Instrumentation follows standard DIC best practice. A global-shutter monochrome CCD/CMOS camera with low noise, high dynamic range, and high quantum efficiency should be used with a telecentric lens. A micrometric slide helps with fine focusing. Cameras and lenses should be mounted rigidly on a well-damped structure decoupled from the load frame to suppress vibration-induced errors, and the camera should be preheated to thermal steady state for 1–2 h before calibration/measurement. Illumination should be intense, cool, and uniform. For DIC readiness, apply a stable, matte, high-contrast speckle over the entire region of interest with ≈ 50 % coverage and speckles ~3×3 to 7×7 px. Perform 2D calibration to assign the pixel scale (mm/px) using a "known-dimension" approach. Acquire an undeformed reference frame before applying load. Use a synchronization to trigger image capture at a consistent phase in the cycle when the crack is maximally open.

To comply with FCGR standards (e.g., ASTM E647 [3]), crack length for da/dN evaluation should be averaged across all present growing cracks because through-thickness asymmetry and left–right differences can bias single-side readings. Practically, this is achieved with multi-camera layouts: for compact-tension specimens, instrument both faces (2 cameras); for middle-tension specimens, instrument both faces of both cracks (4 cameras). Synchronize all cameras to the same phase and process each stream independently with identical settings (parallelized across cores), and then average the resulting crack lengths for FCGR per [3].

Use the 1D DIC extraction via virtual extensometers (VEs) aligned with the expected crack path to obtain CODP curves efficiently in real time, suitable when propagation is approximately straight and out-of-plane motion is negligible. Use the recommended values for user-defined settings: Recommended VE window span is $w_{ve,r} \in \langle 10.0, 14.5 \rangle\ mm$; choose the number of VEs $n_{ve}$ by multiplying the $w_{ve,r}$ by the recommended spatial frequency $f_{ve,r} \in \langle 11, 14 \rangle\ mm^{-1}$. Place the first VE through the notch tip. Use VE length $l_{ve,r} = 1.3\ mm$ to limit crack-subset interference. Subset choice must reflect speckle size/density and the standard trade-offs between noise reduction and spatial resolution. In practice, maintain ~4:1 aspect ratio with the smaller subset dimension along the crack path, e.g., 21×81 px. Use illumination-insensitive correlation criteria (ZNCC/ZNSSD) with sub-pixel interpolation.

Use the fIPMf, which proceeds by detecting the CODP inflection point via Gaussian-process regression to identify the crack tip without thresholds, followed by an adaptive Kalman filter with soft-monotonic refinement to suppress temporal noise and stabilize the time series. In FCGR evaluation, computes $da/dN$ from the synchronized, averaged crack-length histories, assembling points for the da/dN–ΔK curve using the recommended intervalization $\Delta a \geq 0.25$ mm per [3].

Before testing, verify rigid mounting, camera preheat and focus, locked optics, uniform stable illumination (use polarization if needed), absence of heat sources near the optical path, sufficient image contrast and intact speckle, valid calibration and reference frame, applied DIC/sync settings, clean viewing ports, an enabled frame rate compatible with the synchronizer and below the maximal throughput of the IPM (≈ 20 FPS), and prefer added illumination rather than sensor gain. Confirm applicability by avoiding very short initial cracks ($\lesssim 1.5$ mm) where accuracy degrades, and note that validation covers only metallic materials.

At test start, ensure images are not blurred; if blur occurs, shorten exposure and/or increase illumination. Persistent blur may indicate out-of-plane motion exiting the depth of field (DoF); mitigate by constraining motion, refocusing to encompass the excursion, or using a telecentric lens with greater DoF. Confirm that tracked points remain correctly tracked; if not, enlarge subsets and tune correlation/search parameters. For recording, ensure sustained disk write speed matches acquisition (use a fast local SSD), adjust $n_{sync}$ if needed, and check free space. During testing, monitor tracking continuity (guard against lighting changes or accidental bumps), verify straight crack growth without subset interference, and ensure that long-crack growth remains within the VE window $a < (w_{ve,r} - 0.5)\ mm$, so fIPMf retains data on both sides of the inflection

After the test, inspect the crack path for deviations from straightness and any crack–subset interference that could bias results, and confirm paint adhesion without peeling near the crack tip.

# 8 Conclusion

This thesis set out to develop a robust, real-time DIC (digital image correlation) methodology for measuring fatigue crack length that removes the need for threshold tuning—a central weakness of threshold-based approaches such as STM (Strain Threshold Method), whose thresholds are strongly load-dependent and vary across materials or specimen dimensions. In parallel, it sought to replace labor-intensive stop-and-measure VIM (Visual Inspection Method) readings, enabling uninterrupted, automated testing aligned with fatigue crack-growth-rate standards.

The core contribution is a threshold-free, physics-based estimator—the Inflection-Point Method (IPM)—and its fast, filtered implementation (fIPMf). The workflow uses DIC to extract a crack-opening-displacement projection (CODP) curve along the expected crack path; Gaussian-process regression then identifies the CODP inflection corresponding to the crack tip, and an adaptive Kalman filter with soft-monotonicity suppresses synchronization-related temporal noise to stabilize the series. With the optimized scheme (fIPMf), the pipeline reaches ≈20 frames per second—matching STM throughput and exceeding full-field DIC by ~an order of magnitude on the reported hardware.

Extensive validation shows the methodology meets accuracy and robustness requirements for metal-fatigue testing. Using stopped-test frames to validate IPM and the underlying inflection-point principle—thereby avoiding acquisition-timing errors—IPM matches the VIM baseline with RMSE ≈ 31 μm, whereas STM yields RMSE ≈ 274 μm. IPM's load-level sensitivity is negligible relative to STM, supporting applicability in K-decreasing tests. Validation employed a same-side VIM–DIC setup to eliminate through-thickness bias.

For continuously running tests, first validation batch shows that fIPMf estimates crack-growth rates within ~20–30% of a baseline derived from NASGRO-fitted VIM datasets—comparable to variability across the VIM datasets themselves. The second validation batch shows agreement with results reported in the literature with the deviations thoroughly examined and explained in detail.

Sensitivity studies cover DIC and algorithmic parameters. General guidance is provided for case-specific, user-selected settings (e.g., subset size), while quantitative ranges are given where a robust operating window exists (e.g., number of VEs). VE length proved highly influential; a practical working range is identified, and a recommended setting is proposed that balances accuracy and robustness for growth-rate evaluation.

Scope and limitations: accuracy degrades for very short cracks ($\lesssim$ 1.5 mm) due to low-SNR displacements near initiation. The method requires data on both sides of the inflection; operation near the VE-window edge is not recommended. Within these bounds, the optimized pipeline achieves the reported frame rate and stability.

Achievements relative to the stated objectives:

1. **Create a DIC-based methodology for crack-length measurement**: achieved via the IPM → fIPM → fIPMf with adaptive fitting and filtering, plus recommendations on instrumentation and settings.
2. **Validate against a non-DIC baseline (VIM) across materials/sizes/load levels**: completed on paired programs with varying load, thicknesses, materials, and specimen types; the methodology delivers VIM-comparable accuracy in real-time operation.
3. **Compare with another DIC method (STM):** IPM was thoroughly compared with STM; it exceeds STM in accuracy, exhibits substantially lower load dependence, and matches its throughput.
4. **Investigate sensitivity to input parameters**: conducted for DIC parameters (e.g., VE length), test inputs, and IPM settings; yields practical guidance and quantitative ranges where applicable.

In conclusion, the thesis delivers a validated, threshold-free, real-time DIC methodology for assessing fatigue-crack length and growth in metals, avoiding test interruptions, achieving VIM-comparable accuracy during running tests, and surpassing STM with much lower load sensitivity (despite STM's broad adoption). The approach combines an online, adaptive pipeline that learns during acquisition and responds to changes, incorporating monotonicity safeguards for continuous operation, thereby eliminating per-test and per-material threshold tuning. It also validates the inflection-point principle for DIC fatigue testing under uninterrupted operation. All four objectives were met, establishing a practical foundation for extensions to other material classes and deeper automation of fatigue-test workflows.

## References


[1] R. J. Bucci, P. C. Paris, R. W. Hertzberg, R. A. Schmidt, and A. F. Anderson, "Fatigue threshold crack propagation in air and dry argon for a Ti-6Al-4V alloy," *ASTM STP*, vol. 513, pp. 125–140, 1972.

[2] P. Pokorný, T. Vojtek, L. Náhlík, and P. Hutař, "Crack closure in near-threshold fatigue crack propagation in railway axle steel EA4T," *Eng Fract Mech*, vol. 185, pp. 2–19, 2017, doi: 10.1016/j.engfracmech.2017.02.013.

[3] ASTM International, "ASTM E647-23a: Standard Test Method for Measurement of Fatigue Crack Growth Rates," 2023, *ASTM International, 100 Barr Harbor Drive, PO Box C700, West Conshohocken, PA 19428-2959, United States*.

[4] C. M. Stewart and E. Garcia, "Fatigue crack growth of a hot mix asphalt using digital image correlation," *Int J Fatigue*, vol. 120, pp. 254–266, Mar. 2019, doi: 10.1016/j.ijfatigue.2018.11.024.

[5] S. Roux, J. Réthoré, and F. Hild, "Digital image correlation and fracture: an advanced technique for estimating stress intensity factors of 2D and 3D cracks," *J Phys D Appl Phys*, vol. 42, no. 21, p. 214004, Nov. 2009, doi: 10.1088/0022-3727/42/21/214004.

[6] F. Mathieu, F. Hild, and S. Roux, "Identification of a crack propagation law by digital image correlation," *Int J Fatigue*, vol. 36, no. 1, pp. 146–154, Mar. 2012, doi: 10.1016/j.ijfatigue.2011.08.004.

[7] E. Mündecke and V. Mechtcherine, "Tensile behaviour of strain-hardening cement-based composites (SHCC) with steel reinforcing bars," *Cem Concr Compos*, vol. 105, p. 103423, Jan. 2020, doi: 10.1016/j.cemconcomp.2019.103423.

[8] G. Ruocci *et al.*, "Digital Image Correlation and Noise-filtering Approach for the Cracking Assessment of Massive Reinforced Concrete Structures," *Strain*, vol. 52, no. 6, pp. 503–521, Dec. 2016, doi: 10.1111/str.12192.

[9] N. Gehri, J. Mata-Falcón, and W. Kaufmann, "Automated crack detection and measurement based on digital image correlation," *Constr Build Mater*, vol. 256, p. 119383, Sep. 2020, doi: 10.1016/j.conbuildmat.2020.119383.

[10] B. Ščerba, T. Adamec, P. Pokorný, T. Návrat, M. Vajdák, and L. Náhlík, "Inflection point principle combined with digital image correlation and machine learning for crack length measurement in fatigue tests," *Theoretical and Applied Fracture Mechanics*, vol. 139, p. 105052, Oct. 2025, doi: 10.1016/j.tafmec.2025.105052.

[11] D. NOWELL, R. J. H. PAYNTER, and P. F. P. DE MATOS, "Optical methods for measurement of fatigue crack closure: moiré interferometry and digital image correlation," *Fatigue Fract Eng Mater Struct*, vol. 33, no. 12, pp. 778–790, Dec. 2010, doi: 10.1111/j.1460-2695.2010.01447.x.

[12] J. Carroll *et al.*, "Investigation of fatigue crack closure using multiscale image correlation experiments," *Eng Fract Mech*, vol. 76, no. 15, pp. 2384–2398, Oct. 2009, doi: 10.1016/j.engfracmech.2009.08.002.

[13] D. NOWELL, M. E. KARTAL, and P. F. P. DE MATOS, "Digital image correlation measurement of near-tip fatigue crack displacement fields: constant amplitude loading and load history effects," *Fatigue Fract Eng Mater Struct*, vol. 36, no. 1, pp. 3–13, Jan. 2013, doi: 10.1111/j.1460-2695.2012.01707.x.

[14] S. Rabbolini, S. Beretta, and S. Foletti, "Fatigue crack growth in low cycle fatigue: an analysis of crack closure based on image correlation," *Procedia Structural Integrity*, vol. 1, pp. 158–165, 2016, doi: 10.1016/j.prostr.2016.02.022.

[15] L. Patriarca, S. Foletti, and S. Beretta, "A comparison of DIC-based techniques to measure crack closure in LCF," *Theoretical and Applied Fracture Mechanics*, vol. 98, pp. 230–243, Dec. 2018, doi: 10.1016/j.tafmec.2018.09.020.

[16] Imetrum, "Crack Length Gauge: identifying the threshold value for DCB specimens," 2022. Accessed: Dec. 02, 2023. [Online]. Available: https://support.imetrum.com/support/solutions/articles/80001044765-

crack-length-gauge-identifying-the-threshold-value-for-dcb-specimens

[17] X-Sight, “ALPHA DIC SOFTWARE MODULES: CRACK PROBE.” Accessed: Dec. 02, 2023. [Online]. Available: https://www.xsight.eu/alpha-digital-image-correlation-software-modules/#CL

[18] G. I. Barenblatt, “The Mathematical Theory of Equilibrium Cracks in Brittle Fracture,” *Advances in Applied Mechanics*, vol. 7, pp. 55–129, 1962, doi: https://doi.org/10.1016/S0065-2156(08)70121-2.

[19] D. S. Dugdale, “Yielding of steel sheets containing slits,” *J Mech Phys Solids*, vol. 8, no. 2, pp. 100–104, May 1960, doi: 10.1016/0022-5096(60)90013-2.

[20] J. J. Zhang, “Chapter 4 - Basic rock fracture mechanics,” in *Applied Petroleum Geomechanics*, J. J. Zhang, Ed., Gulf Professional Publishing, 2019, pp. 133–161. doi: https://doi.org/10.1016/B978-0-12-814814-3.00004-6.

[21] G. Sciarra and S. Vidoli, “Asymptotic Fracture Modes in Strain-Gradient Elasticity: Size Effects and Characteristic Lengths for Isotropic Materials,” *J Elast*, vol. 113, no. 1, pp. 27–53, Sep. 2013, doi: 10.1007/s10659-012-9409-y.

[22] P. Skalka, P. Navrátil, and M. Kotoul, “Novel approach to FE solution of crack problems in the Laplacian-based gradient elasticity,” *Mechanics of Materials*, vol. 95, pp. 28–48, Apr. 2016, doi: 10.1016/j.mechmat.2015.12.007.

[23] M. Kotoul *et al.*, “Ab initio aided strain gradient elasticity theory in prediction of nanocomponent fracture,” *Mechanics of Materials*, vol. 136, p. 103074, Sep. 2019, doi: 10.1016/j.mechmat.2019.103074.

[24] A. Gosch, J. Geier, F. Arbeiter, M. Berer, and G. Pinter, “Methods for automated crack length detection in fracture mechanical fatigue tests of unreinforced polymers,” *Procedia Structural Integrity*, vol. 28, pp. 1184–1192, 2020, doi: 10.1016/j.prostr.2020.11.100.

[25] V. Plevris, G. Solorzano, N. P. Bakas, and M. E. A. Ben Seghier, “Investigation of performance metrics in regression analysis and machine learning-based prediction models,” European Community on Computational Methods in Applied Sciences, 2022. doi: 10.23967/eccomas.2022.155.

[26] R. G. Forman and S. R. Mettu, “Behavior of surface and corner cracks subjected to tensile and bending loads in Ti-6Al-4V alloy,” Aug. 1990. [Online]. Available: https://www.osti.gov/biblio/5555321

[27] T. L. Anderson, *Fracture Mechanics: Fundamentals and Applications, Third Edition*, 3rd ed. CRC Press, 2005.

[28] T. Comlekci, J. M. Pérez, L. Milne, Y. Gorash, and D. Mackenzie, “Structural steel crack propagation experimental and numerical analysis,” *Procedia Structural Integrity*, vol. 42, pp. 694–701, 2022, doi: 10.1016/j.prostr.2022.12.088.

[29] S. Seitl, P. Pokorný, P. Miarka, J. Klusák, Z. Kala, and L. Kunz, “Comparison of fatigue crack propagation behaviour in two steel grades S235, S355 and a steel from old crane way,” *MATEC Web of Conferences*, vol. 310, p. 00034, Mar. 2020, doi: 10.1051/matecconf/202031000034.

[30] S. Seitl, P. Pokorný, J. Klusák, S. Duda, and G. Lesiuk, “Effect of Specimen Thickness on Fatigue Crack Growth Resistance in Paris Region in AISI 304 STEEL,” 2022, pp. 291–297. doi: 10.1007/978-3-030-97822-8_34.

[31] N. Nagaishi, M. Yoshikawa, S. Okazaki, J. Yamabe, F. Yoshida, and H. Matsunaga, “Evaluation of fatigue life and fatigue limit of circumferentially-notched Type 304 stainless steel in air and hydrogen gas based on crack-growth property and cyclic stress-strain response,” *Eng Fract Mech*, vol. 215, pp. 164–177, Jun. 2019, doi: 10.1016/j.engfracmech.2019.05.005.

# Author's Curriculum Vitae

## Education

| | |
|---|---|
| 2020 – present | Brno University of Technology, Faculty of Mechanical Engineering<br>Doctoral study, Programme: Applied Mechanics |
| 2018 – 2020 | Brno University of Technology, Faculty of Mechanical Engineering<br>Master's study, Specialization: Engineering Mechanics and Biomechanics |
| 2015 – 2018 | Brno University of Technology, Faculty of Mechanical Engineering<br>Bachelor's study, Specialization: Fundamentals of Mechanical Engineering |
| 2007 – 2015 | Secondary Grammar School, Český Těšín, Frýdecká 689/30 |

## Work Experience

| | |
|---|---|
| 09/2024 – present | X-Sight s.r.o<br>Sales and Development Engineer |
| 05/2021 – 06/2024 | Brno University of Technology, Faculty of Mechanical Engineering, Institute of Solid Mechanics, Mechatronics and Biomechanics, Department of Engineering Mechanics<br>Researcher |
| 08/2020 – 02/2021 | Garrett Motion Czech Republic s.r.o.<br>FEA Engineer |
| 06/2019 – 07/2020 | Garrett Motion Czech Republic s.r.o.<br>Student FEA Engineer |
| 06/2017 – 08/2019 | BOMAR, s r.o.<br>Assistant Design Engineer |

## Achievements & Awards

| | |
|---|---|
| 12/2018 | Winner of "8 z VUT" – Brno University of Technology's Best Bachelor's Thesis |
| 09/2022 | 3rd Place, Young Scientist Presentation Award, Danubia-Adria Symposium |

## Skills

| | |
|---|---|
| Languages | Czech (Mother Tongue)<br>English (Advanced)<br>French, Deutch, Polish (Basic) |
| Software | Python (Intermediate), C# (Basic), VBA (Basic/Intermediate)<br>Ansys Workbench/APDL (Intermediate), Abaqus (Basic)<br>Autodesk Inventor, Autodesk Fusion 360 (Intermediate), Creo (basic)<br>Alpha DIC (Advanced)<br>Prusa3D (Intermediate)<br>Microsoft Word, Excel, Outlook, Visio … (Intermediate) |
| Driver's license | Class B |

## Abstract

Stopping fatigue tests for visual readings is labor-intensive and conflicts with uninterrupted acquisition recommended in fatigue crack growth rate standards. Furthermore, measuring fatigue crack length during ongoing tests reduces operator workload and enables automation. This thesis develops a digital image correlation (DIC)–based methodology that replaces visual inspection with a traveling microscope (VIM) and validates it against VIM data across materials, specimen sizes and types, and load levels, while also comparing it with a DIC thresholding approach, the Strain threshold method (STM). Sensitivity to input parameters is analyzed, limitations are identified, and user recommendations are formulated. The core estimator is a physics-based Inflection point method (IPM) and its fast, filtered implementation (fIPMf).

The workflow is as follows. DIC provides displacements via software-defined "virtual extensometers" laid out along the expected crack path. The resulting curve is a projection of crack opening displacements. Gaussian Process Regression—used here to mitigate spatial noise—fits this curve, and the inflection point of the fitted curve is taken as the crack tip (IPM). Its fast implementation (fIPM) restructures processing and reduces computation time by 55%; the filtered variant (fIPMf) adds an adaptive Kalman filter with a soft-monotonicity safeguard to stabilize the time series, reducing temporal noise by about an order of magnitude to sub-micrometer levels.

Validation used compact tension and middle tension specimens, with all the methods (VIM, IPM, and STM) applied to the same images acquired from the same side of the specimen, removing through-thickness bias from unequal crack lengths. The first validation compared crack-length results on images acquired during test stoppages. In this setting, IPM matched the VIM baseline with a root-mean-square error (RMSE) of 31 μm, while STM reached 274 μm. The most important sensitivity finding was the negligible load dependence of IPM, in contrast to STM.

An additional validation compared crack-growth-rate results from VIM and fIPMf on the same samples measured sequentially. VIM data were fitted with the NASGRO equation and used as a baseline; fIPMf results deviated by approximately 20-30%, which is comparable to the spread among VIM datasets themselves. For real-time use, fIPMf offers the same data-processing frequency as STM, which is more than 10× higher than for full-field DIC.

In summary, the proposed methodology enables non-interruptive, VIM-comparable crack-length and crack-growth evaluation during running tests and outperforms STM by a large margin. It offers a processing speed of about 20 frames/s. Key benefits include a threshold-free, physics-based estimator; robust adaptive fitting and filtering that learn during the test and react to changing conditions; and negligible load-level sensitivity, enabling K-decreasing tests to identify the stress intensity factor threshold—something difficult with STM.

## Abstrakt

Zastavování únavových zkoušek kvůli vizuálním odečtům je pracné a je v rozporu s nepřetržitým snímáním doporučovaným normami pro stanovení rychlosti růstu únavových trhlin. Měření délky únavové trhliny v průběhu zkoušky navíc snižuje zátěž obsluhy a umožňuje automatizaci. Tato práce rozvíjí metodiku založenou na korelaci digitálních obrazů (DIC), která nahrazuje vizuální inspekci pomocí posuvného mikroskopu (VIM) a validuje ji vůči datům VIM napříč materiály, velikostmi a typy vzorků i úrovněmi zatížení; současně ji porovnává s prahovým přístupem na DIC datech, metodou prahového přetvoření (STM). Je analyzována citlivost na vstupní parametry, jsou identifikována omezení a formulovány uživatelská doporučení. Jádrem metodiky je fyzikálně podložený odhad délky trhliny – metoda inflexního bodu (IPM) – a její rychlá implementace (fIPM) a filtrovaná varianta (fIPMf).

Postup je následující. DIC poskytuje posuvy prostřednictvím softwarově definovaných „virtuálních extenzometrů“ rozmístěných podél očekávané trajektorie trhliny. Výsledná křivka představuje projekci otevření trhliny. Regrese pomocí gaussovských procesů tuto křivku prokládá a inflexní bod proložené křivky je považován za čelo trhliny (IPM). Rychlá implementace metody inflexního bodu (fIPM) mění procesní schéma, čímž zkracuje výpočetní čas o 55 %. Filtrovaná varianta (fIPMf) přidává adaptivní Kalmanův filtr s měkkým vynucením monotonicity pro stabilizaci časové řady, čímž snižuje šum přibližně o řád na submikrometrickou úroveň.

Validace využila zkušební tělesa typu CT a M(T). Všechny metody (VIM, IPM a STM) byly aplikovány na stejné snímky pořízené ze stejné strany vzorku, čímž se eliminovalo zkreslení přes tloušťku způsobené nestejnými délkami trhlin. První validace porovnávala výsledky délky trhliny na snímcích pořízených při přerušeních zkoušky. V tomto uspořádání se výsledky IPM shodovaly s referencí VIM (RMSE 31 μm), zatímco výsledky STM se od reference řádově lišily (RMSE 274 μm). Nejdůležitějším zjištěním z analýzy citlivosti byla zanedbatelná závislost IPM na zatížení, na rozdíl od STM.

Další validace porovnala výsledky rychlosti růstu trhliny z VIM a fIPMf na stejných vzorcích měřených sekvenčně, nejdříve pomocí VIM, pak s využitím fIPMf. Data získaná z VIM byla proložena rovnicí NASGRO a použita jako reference; výsledky fIPMf se odchylovaly přibližně o 20–30 %, což je srovnatelné s rozptylem mezi samotnými datovými sadami VIM. Pro použití v reálném čase nabízí fIPMf stejnou frekvenci zpracování dat jako STM, což je více než 10× vyšší než u full-field DIC.

Navržená metodika umožňuje nepřerušované vyhodnocování délky a růstu trhliny během probíhajících zkoušek s přesností srovnatelnou s VIM a výrazně přesnějšími výsledky oproti STM. Nabízí rychlost zpracování okolo 20 snímků/s. Klíčové přínosy zahrnují bezprahový, fyzikálně podložený odhad; robustní adaptivní prokládání a filtrování, které se v průběhu zkoušky učí a reagují na měnící se podmínky; a zanedbatelnou citlivost na úroveň zatížení, jež umožňuje provádět zkoušky s klesajícím rozkmitem faktoru intenzity napětí ($\Delta K$) používané k určení prahové hodnoty součinitele intenzity napětí ($\Delta K_{th}$) — což je u STM velmi obtížné.